ACS OMEGA

http://pubs.acs.org/journal/acsodf

Article

Blue Photoluminescence and Cyan-Colored Afterglow of Undoped $SrSO_4$ Nanoplates

Bao-gai Zhai, Hanfei Xu, Qing Zhang, and Yuan Ming Huang*

Cite This: *ACS Omega* 2021, 6, 10129−10140

Read Online

ACCESS | Metrics & More | Article Recommendations | Supporting Information

ABSTRACT: Undoped $SrSO_4$ nanoplates were synthesized *via* the composite hydroxide-mediated approach. The products were characterized by means of X-ray diffractometry, scanning electron microscopy, X-ray energy-dispersive spectroscopy, X-ray photoelectron spectroscopy, photoluminescence (PL) spectroscopy, electron spin resonance technique, afterglow spectroscopy, and thermoluminescence dosimetry. The steady-state PL spectrum of undoped $SrSO_4$ nanoplates can be deconvoluted into two distinct Gaussian bands centered at 2.97 eV (417.2 nm) and 2.56 eV (484.4 nm), respectively. The nature of the defect emissions is confirmed through the emission-wavelength-dependent PL decays as well as the excitation-wavelength-dependent PL decays. A cyan-colored afterglow from undoped $SrSO_4$ nanoplates can be observed with naked eyes in the dark, and the afterglow spectrum of the undoped $SrSO_4$ nanoplates exhibits a peak at about 492 nm (2.52 eV). The duration of the afterglow is measured to be 16 s. The thermoluminescence glow curve of the undoped $SrSO_4$ nanoplates shows a peak at about 40.1 °C. The trapping parameters are determined with the peak shape method, the calculated value of the trap depth is 0.918 eV, and the frequency factor is 1.2×10^{14} s^{-1}. Using density functional calculations, the band structures and densities of states of oxygen-deficient $SrSO_4$ and strontium-deficient $SrSO_4$ are presented. The mechanisms of the cyan-colored afterglow are discussed for undoped $SrSO_4$, and the oxygen vacancies in $SrSO_4$ are proposed to be the luminescence center of the afterglow.

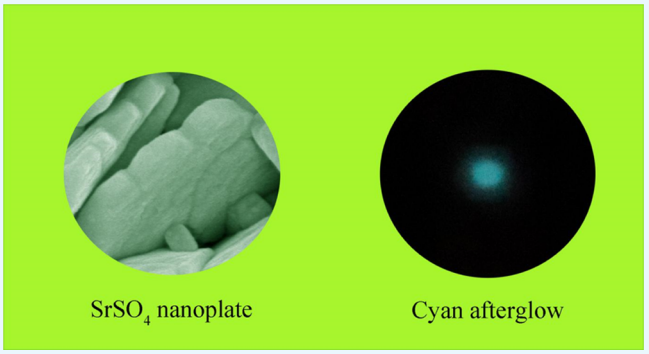

1. INTRODUCTION

Afterglow materials are materials that continue to emit light after the removal of the excitation source.[1] The new era of afterglow materials came when long-lasting afterglow of Eu^{2+}- and Dy^{3+}-codoped $SrAl_2O_4$ was reported in 1996.[2] Since then, intensive research activities have been focused on rare-earth doped alkaline-earth aluminates (MAl_2O_4, M = Mg, Ca, Sr, and Ba) due to their advantages of long afterglow duration, high light intensity, and non-toxicity.[3−8] However, these afterglow materials exhibit poor resistance to moisture and water due to the hydrolysis of aluminates. Apparently, it is of significance to develop water-resistant afterglow materials in order to meet the increasing demand on water-resistant afterglow materials for outdoor applications.

An essential prerequisite of water-resistant afterglow materials is that host materials are poorly soluble in water. With the solubility of 1 part in 8800, strontium sulfate ($SrSO_4$) is poorly soluble in water. The low aqueous solubility and low toxicity make $SrSO_4$ an ideal candidate for water-resistant afterglow materials provided that $SrSO_4$ can display afterglow. We have noticed that some undoped inorganic materials can give off afterglows. For instance, a blue afterglow peaking at 480−490 nm was reported for undoped HfO_2,[9,10] and a blue afterglow peaking at 498 nm was reported for undoped inverse spinel Mg_2SnO_4.[11] Additionally, a blue afterglow peaking at about 440 nm has been recently reported for undoped $CaAl_2O_4$ nanocrystals.[12,13] These reports indicate that an alternative strategy toward designing water-resistant afterglow materials is through the examination of water-insoluble undoped inorganic materials. However, the afterglow characteristics of undoped $SrSO_4$ are not reported yet. In this paper, the afterglow properties of undoped $SrSO_4$ nanoplates are presented. The mechanisms of the cyan-colored afterglow are discussed for undoped $SrSO_4$. Our results demonstrate that the oxygen vacancies in the oxide are responsible for the observed afterglow in undoped $SrSO_4$. This work aims at shedding light on the origin of the blue photoluminescence (PL) and providing a comprehensive understanding on the mechanisms of cyan-colored afterglow from water-insoluble undoped $SrSO_4$.

Received: January 12, 2021
Accepted: March 31, 2021
Published: April 8, 2021

2. RESULTS AND DISCUSSION

2.1. Phase and Morphology of Undoped $SrSO_4$. Figure 1 depicts the XRD pattern of the undoped $SrSO_4$ nanoplates.

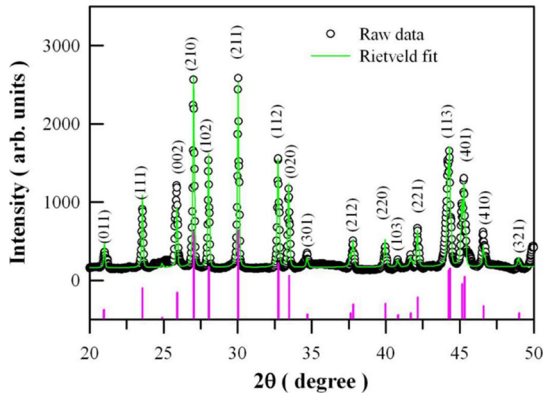

Figure 1. XRD curve and its Rietveld analysis of the undoped $SrSO_4$ nanoplates. Open circles: raw data; solid green curve: Rietveld diffractogram. The standard diffraction data of $SrSO_4$ (JCPDS no. 05-0593) are displayed at the bottom for comparison.

The open circles (in black) in Figure 1 represent the raw XRD data of the undoped $SrSO_4$ nanoplates. As can be seen in Figure 1, the XRD profile of the undoped $SrSO_4$ nanoplates exhibits distinct peaks at 20.984, 23.579, 25.932, 27.039, 28.063, 30.043, 32.765, 33.484, 34.714, 37.817, 39.984, 40.835, 42.173, 44.346, 45.329, 46.610, and 49.013°. For comparison, the standard diffraction data of $SrSO_4$, which are available in a data file provided by the Joint Committee on Powder Diffraction Standards (JCPDS) as JCPDS no. 05-0593, are displayed at the bottom by the vertical bars (in pink). According to JCPDS no. 05-0593, these peaks can be assigned to the reflections from the (011), (111), (002), (210), (102), (211), (112), (020), (301), (212), (220), (103), (221), (113), (401), (410), and (321) crystallographic planes of $SrSO_4$.[14,15] Some of the diffraction peaks in Figure 1 are marked with Miller indices. Obviously, the XRD data in Figure 1 confirm the formation of orthorhombic $SrSO_4$ *via* the composite hydroxide-mediated approach.

Being widely used in the field of powder XRD, Rietveld analysis is an effective method to determine the crystal structures and lattice parameters for a large diversity of crystals. Rietveld analysis was performed through the wide pattern fitting of the XRD pattern in Figure 1. The program FULLPROF Suite 2014 was used to perform the Rietveld refinement. The solid green curve in Figure 1 shows the Rietveld diffractogram of the undoped $SrSO_4$ nanoplates. The refined unit cell parameters for the undoped $SrSO_4$ nanoplates are a = 0.8361 nm, b = 0.5351 nm, and c = 0.6871 nm with the unit cell volume of 0.3072 nm^3. Apparently, the lattice parameters derived from our $SrSO_4$ nanoplates are very close to those of $SrSO_4$ in the standard file (ICSD 85808) whose a = 0.8359 nm, b = 0.5351 nm, and c = 0.6869 nm.

Figure 2 depicts the SEM micrographs of undoped $SrSO_4$. As shown in Figure 2, we can see clearly that $SrSO_4$ nanoplates are formed *via* the composite hydroxide-mediated approach, and the typical thickness of the undoped $SrSO_4$ nanoplates is around 80 nm. However, the other two lateral dimensions of the nanoplates vary in the range of 200−800 nm. For example, the length and width of the nanoplate marked in Figure 2 are about 543 and 200 nm, respectively. As documented in the

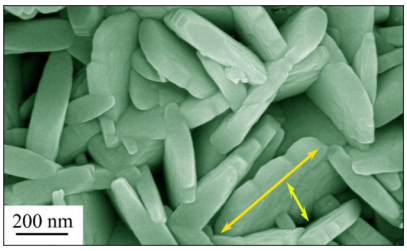

Figure 2. SEM micrograph of the undoped $SrSO_4$ nanoplates.

literature, the composite hydroxide-mediated approach is a powerful methodology for creating a diversity of nanostructures.[16,17] For instance, Eu^{2+}-doped $SrSO_4$ nanostructures in the morphology of nanoneedle, nanorod, octagonal disk, and hexagonal disks were synthesized *via* the hydrothermal approach,[15] but $SrSO_4$ in the morphology of nanoplates was not reported yet. Thus, our undoped $SrSO_4$ nanoplates are unique in their morphology.

Figure 3 depicts the EDX spectrum of the undoped $SrSO_4$ nanoplates. As can be seen in Figure 3, the three X-ray

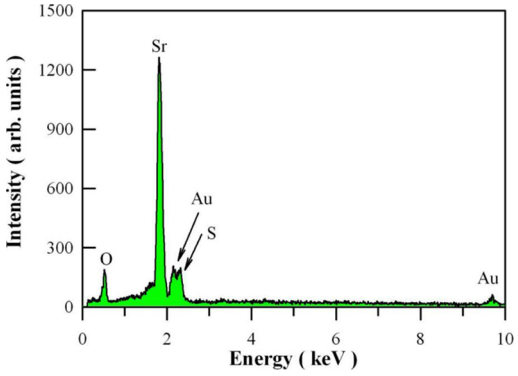

Figure 3. EDX spectrum of the undoped $SrSO_4$ nanoplates.

emission peaks in the EDX spectrum are located at 0.53, 1.81, and 2.31 keV, which can be attributed to the characteristic X-ray emissions of O($K\alpha_1$), Sr($L\alpha_{1,2}$), and S($K\alpha_{1,2}$), respectively. In addition to those peaks, the X-ray emissions of Au($M\alpha_1$) and Au($L\alpha_1$) can also be identified at 2.122 and 9.713 keV, respectively. As described previously, the Au element in the specimen was introduced in the process of Au sputtering for the convenience of SEM characterization.[3,18] As expected, the EDX spectrum of undoped $SrSO_4$ confirms that elements Sr, S, and O are present in our synthesized compound.

2.2. XPS Spectrum of Undoped $SrSO_4$. Figure 4 illustrates the XPS survey scan (a), XPS spectra of S 2p (b), Sr 3d (c), and O 1s (d) in $SrSO_4$ nanoplates. Obviously, the photoelectron lines of S 2p, O 1s, and Sr 3d can be identified in Figure 4a, which confirms the presence of elements S, O, and Sr in our target compound $SrSO_4$ nanoplates. The peak of S $2p_{3/2}$ in Figure 4b is located at 168.98 eV. According to the report by Vasquez, the photoelectron line of S $2p_{3/2}$ in $SrSO_4$ is located at 168.75 eV.[19] Thus, our recorded photoelectron line of S $2p_{3/2}$ is very close to that documented in the literature. The binding energy peak of Sr $3d_{5/2}$ can be derived from Figure 4c. As shown in Figure 4c, the binding energy peak of Sr $3d_{5/2}$ is located at 133.68 eV. When compared to the peak of Sr $3d_{5/2}$ (133.85 eV) in the $SrSO_4$ nanofilm, the peak of Sr $3d_{5/2}$ in our undoped $SrSO_4$ nanoplates is shifted 0.17 eV toward the

https://doi.org/10.1021/acsomega.1c00194
ACS Omega 2021, 6, 10129−10140

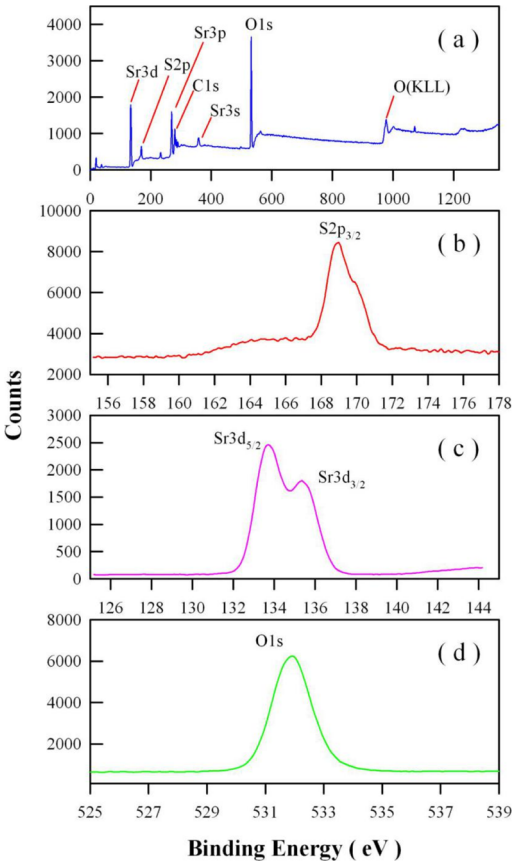

Figure 4. XPS survey scan (a), XPS spectra of S 2p (b), Sr 3d (c), and O 1s (d) in $SrSO_4$ nanoplates.

lower binding energy.[20] Interestingly, in Figure 4c, we also recorded a photoelectron line at 135.38 eV, which can be tentatively attributed to the binding energy peak of Sr $3d_{3/2}$. Finally, the XPS spectral profile of O 1s is displayed in Figure 4d. As can be seen in Figure 4d, the XPS spectral profile of O 1s is located at 531.88 eV, which is very close to the reported values of 531.8 and 531.9 eV for $SrSO_4$ by Vasquez.[19,20] Obviously, it is hard to deconvolute this high-resolution XPS spectrum of O 1s into two components. Generally speaking, the high-resolution XPS spectrum of O 1s can be deconvoluted into two components if the population density of oxygen vacancy in $SrSO_4$ is high enough since the chemical environment of Sr−O bond in perfect $SrSO_4$ is different from that in oxygen-deficient $SrSO_4$. Thus, the data in Figure 4d suggest that the population density of oxygen vacancy in the $SrSO_4$ matrix is not sufficiently high.

2.3. Steady-State PL Spectrum of Undoped $SrSO_4$. Figure 5 illustrates the PL spectrum of the undoped $SrSO_4$ nanoplates in the energy scale. The hollow circles in Figure 5 represent the raw PL data. Apparently, this broad PL spectrum can be deconvoluted into two Gaussian bands. The first Gaussian band, as shown by the blue curve in Figure 5, is peaked at 2.97 eV (417.5 nm). The second Gaussian band, as shown by the green curve in Figure 5, is centered at 2.56 eV (484.4 nm). For clarity, the former PL band is denoted as PL band A, while the latter PL band is denoted as PL band B. The area ratio of the two PL bands A to B is 1.42:1. By using the techniques reported earlier,[21] the Commission Internationale de l'Eclairage (CIE) chromaticity coordinates of the undoped

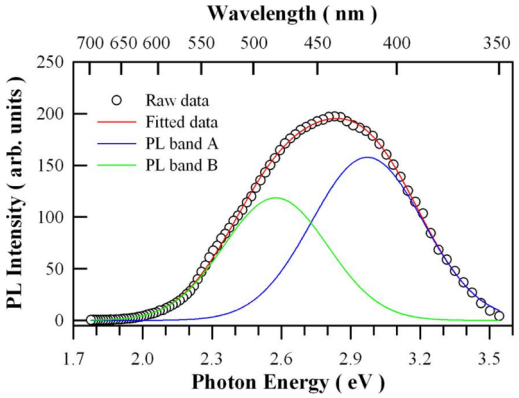

Figure 5. PL spectrum of the undoped $SrSO_4$ nanoplates in energy scale and its Gaussian band deconvolution.

$SrSO_4$ are calculated to be (0.167, 0.197), and the PL color of the undoped $SrSO_4$ nanoplates is identified as blue.

$SrSO_4$, which is a typical insulator with a band gap of around 7.6 eV,[22] is often utilized as the host material of rare-earth dopants to develop efficient luminescent materials. Due to the large band gap of $SrSO_4$, the photon energy of our ultraviolet laser (3.82 eV) is not high enough to pump carriers from its valence band to conduction band. As a result, the two PL sub-bands in Figure 5 cannot originate from the band-to-band recombination.[14] Thus, the two PL bands are very likely connected with intrinsic defects in $SrSO_4$. Examples of the intrinsic defects in $SrSO_4$ include oxygen and strontium vacancies, oxygen and strontium interstitials, and oxygen and strontium antisites. After having considered the high formation energies of antisites and interstitials, only the oxygen vacancies and the strontium vacancies are the most probable intrinsic defects in $SrSO_4$. The oxygen vacancy is generally known to be one of the important intrinsic defects in oxides, and the oxygen vacancy-related emissions are documented for a large diversity of host materials such as $CaAl_2O_4$,[12,13] $SrAl_2O_4$,[4−6] $BaAl_2O_4$,[8] $SrSO_4$,[14] $ZnWO_4$,[23,24] and $ZnMoO_4$.[25] Consequently, the two PL bands A and B in Figure 5 can be attributed to the oxygen and strontium vacancies in $SrSO_4$.

2.4. Afterglow Spectrum and Afterglow Decay Profile of Undoped $SrSO_4$. The afterglow spectrum of undoped $SrSO_4$ nanocrystals is shown in Figure 6a. As can be seen in Figure 6a, the peak position of this afterglow spectrum is located at 492 nm (2.52 eV). This afterglow spectrum spans across a wide spectral range from 375 to 625 nm, but the profile of this afterglow spectrum is relatively narrow when compared to the PL spectrum of the undoped $SrSO_4$ nanoplates in Figure 5. Obviously, one part of this afterglow spectrum falls into the blue spectral regime, while the other part of this spectrum falls into the green spectral regime. Generally speaking, green and blue mix to produce cyan. According to the method described in our previous work,[21,23] the CIE chromaticity coordinates of the afterglow are derived to be (0.124, 0.327), and the calculated value of its color temperature is 24659 K. As a result, the color of the afterglow can be depicted as cyan. The inset in Figure 6a depicts the afterglow photo of the undoped $SrSO_4$ nanoplates. Indeed, the color of the afterglow is cyan. The afterglow decay curve of undoped $SrSO_4$ is presented in Figure 6b. As shown in Figure 6b, this decay curve exhibits that the cyan-colored afterglow of undoped $SrSO_4$ can last for about 16 s. Although it is many times shorter than those of rare-earth doped $SrAl_2O_4$ and

https://doi.org/10.1021/acsomega.1c00194
ACS Omega 2021, 6, 10129−10140

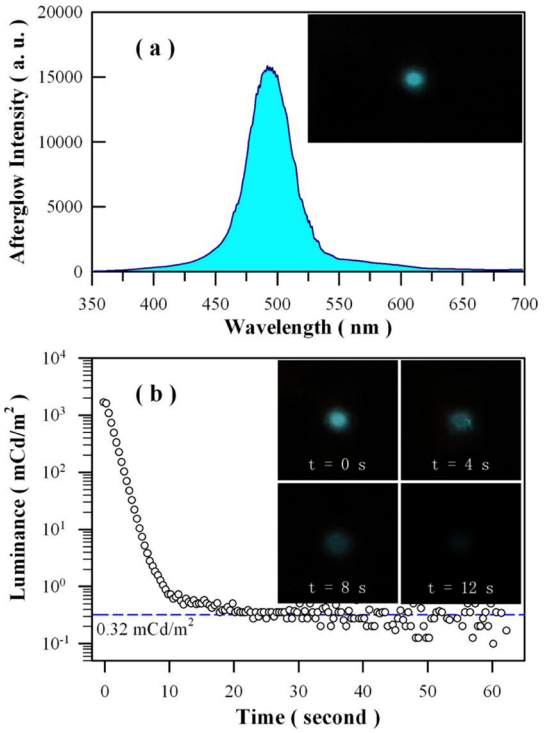

Figure 6. (a) Afterglow spectrum of the undoped $SrSO_4$ nanoplates. (b) Afterglow decay profile of the undoped $SrSO_4$ nanoplates. Inset in (a): afterglow photo of the undoped $SrSO_4$ nanoplates. Inset in (b): afterglow photos of the undoped $SrSO_4$ nanoplates at 0, 4, 8, and 12 s after the extinction of excitation.

$BaAl_2O_4$,[4−6,8] the duration of the cyan-colored afterglow of undoped $SrSO_4$ is in the same order of those of undoped $CaAl_2O_4$, undoped HfO_2, and undoped $Mg(Mg,Sn)O_4$.[9−13]

Although $SrSO_4$ is an excellent host material of rare-earth dopants to develop efficient phosphors, neither rare-earth-doped $SrSO_4$ nor undoped $SrSO_4$ was reported to give off afterglow. Therefore, the key issue is why undoped $SrSO_4$ can exhibit the cyan-colored afterglow. A comparison of Figure 6a with Figure 5 reveals that the peak energy of the afterglow spectrum (2.52 eV) in Figure 6 is very close to that of PL band B in Figure 5 (2.56 eV). This fact suggests that the blue afterglow of undoped $SrSO_4$ is likely correlated with the intrinsic defects in $SrSO_4$. Actually, oxygen vacancies are proposed as the luminescence center of the afterglow in undoped $CaAl_2O_4$,[12,13] undoped HfO_2,[9,10] and undoped inverse spinel Mg_2SnO_4.[11] Moreover, Zhou et al. recently reported blue afterglow from undoped boron oxide.[26] Thus, the knowledge on defect energy levels of intrinsic defects, particularly the oxygen and strontium vacancies, in $SrSO_4$ can help in understanding the origin of cyan afterglow of $SrSO_4$.

Both the PL and afterglow of these $SrSO_4$ nanoplates appear to be fairly stable after being stored in moisture for 2 years. Interestingly, both the afterglow intensity and the lifetime of $SrSO_4$ nanoplates are found to be chemically stable when the phosphor is in contact with acidic solutions (hydrochloric acid) and basic solutions (sodium hydroxide). Such advantages over aluminate-based afterglow materials can attract considerable attention due to the outstanding chemical stability of $SrSO_4$. Furthermore, we checked the thermal stability of the afterglow of undoped $SrSO_4$ by annealing the phosphors at 200, 300, 400, 500, 600, and 700 °C. The duration of each annealing was 2 h. The afterglow photos of undoped $SrSO_4$ after annealing at different temperatures are given in Figure S1. Both the afterglow intensity and the afterglow duration of undoped $SrSO_4$ are found to increase monotonically with the annealing temperature up to 400 °C. After having reached their apex, both the afterglow intensity and the afterglow duration turn their heads down as the annealing temperature increases from 500 to 700 °C. In particular, the afterglow of undoped $SrSO_4$ becomes quenched after annealing at 700 °C for 2 h. Additionally, we measured the PL spectra of undoped $SrSO_4$ nanoplates at 200, 300, 400, and 500 °C on a heating console. As shown in Figure S2, the integrated PL intensity of undoped $SrSO_4$ nanoplates is quite stable as the temperature of the heating console varies from 200 to 400 °C. As a contrast, the integrated PL intensity of undoped $SrSO_4$ nanoplates is severely degraded when the temperature of the heating console is increased to 500 °C.

2.5. Electronic Structures of Strontium-Deficient $SrSO_4$ and Oxygen-Deficient $SrSO_4$. To get better insights into this problem, accurate calculations on the band structures and densities of states are required for defect-bearing $SrSO_4$. Figure 7 represents the density functional theory calculated band structures and densities of states of oxygen-deficient $SrSO_4$ (*i.e.*, $SrSO_{4-\delta}$, where δ = 0.0625). In the density functional calculations, the exchange−correlation functional was treated within the GGA + *U* scheme by the Perdew−Burke−Ernzerhof potential. The U parameter was selected as U^{2p} = 4 eV for oxygen. As shown in Figure 7, the calculated band gap of the oxygen-deficient $SrSO_4$ is 7.23 eV. It is found that the oxygen vacancy can introduce two defect energy levels

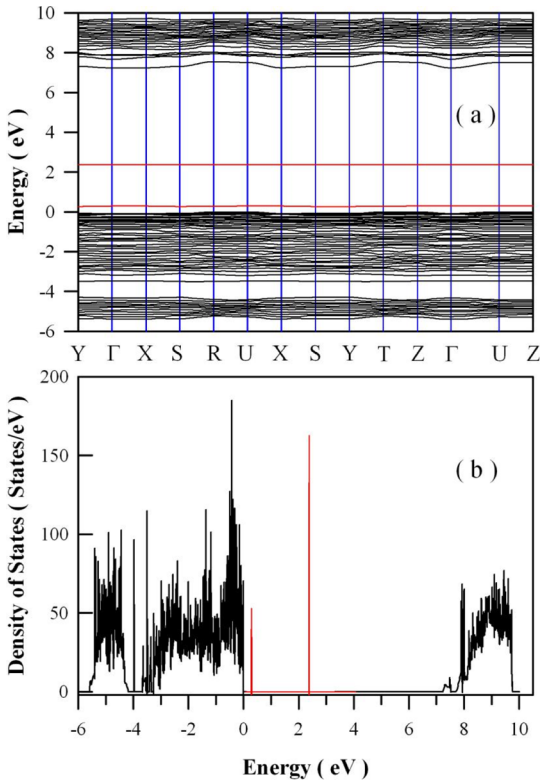

Figure 7. Density functional theory calculated band structures (a) and density of states (b) of oxygen-deficient $SrSO_4$ (*i.e.*, $SrSO_{4-\delta}$, where δ = 0.0625). The exchange−correlation functional was treated within the GGA + *U* scheme by the Perdew−Burke−Ernzerhof potential. The U parameter was selected as U^{2p} = 4 eV for oxygen.

https://doi.org/10.1021/acsomega.1c00194
ACS Omega 2021, 6, 10129−10140

in the band gap of $SrSO_4$, one of which is located at E_V + 2.38 eV, while the other is located at E_v + 0.30 eV. These defect energy levels can be clearly identified in the density of states, as shown in Figure 7b. Apparently, our calculated band gap value of $SrSO_4$ is underestimated when compared to the experimental band gap value of 7.6 eV for $SrSO_4$.[22] The density functional calculations are often known to underestimate the band gap value of materials. For example, Zhai et al. reported that $SrSO_4$ is an insulator with an indirect band gap of 6.14 eV using the GGA approach in the density functional calculations.[14] Hu et al. reported that the indirect band gap of $SrSO_4$ is 6.0 eV using the plane-wave pseudopotential GGA approach.[27] Using the scissors operator to overcome this underestimation, the band gap of oxygen-deficient $SrSO_4$ is adjusted to be 7.6 eV; meanwhile, the oxygen vacancy-introduced defect energy levels are adjusted to E_V + 2.50 eV and E_V + 0.31 eV.

Figure 8 represents the density functional theory calculated band structures and densities of states of strontium-deficient

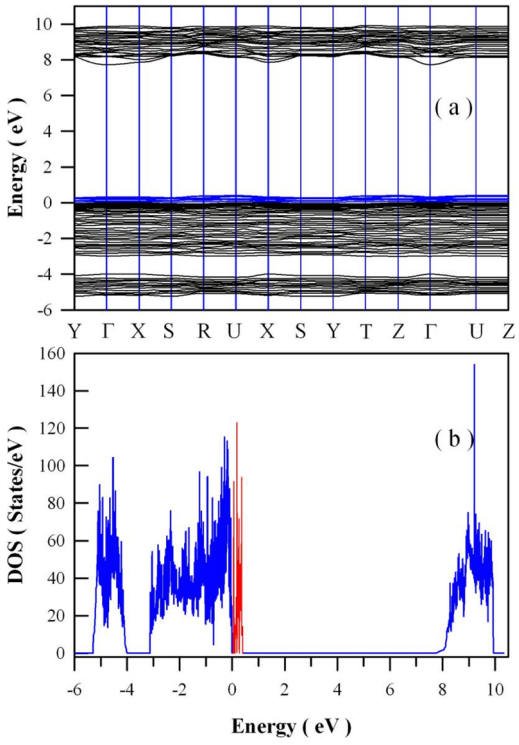

Figure 8. Density functional theory calculated band structures (a) and density of states (b) of Sr-deficient $SrSO_4$ (*i.e.*, $Sr_{1-\delta}SO_4$, where δ = 0.0625). The exchange−correlation functional was treated within the GGA + U scheme by the Perdew−Burke−Ernzerhof potential. The U parameter was selected as U^{2p} = 4 eV for oxygen.

$SrSO_4$ (*i.e.*, $Sr_{1-\delta}SO_4$, where δ = 0.0625). As shown in Figure 8, the calculated band gap of strontium-deficient $SrSO_4$ is 7.72 eV, which is slightly larger than the reported band gap value of 7.6 eV for $SrSO_4$.[22,27] Obviously, the defect energy levels of strontium-deficient $SrSO_4$ are very close to the top of the valence band of $SrSO_4$. Detailed analysis reveals that the peak of these defect energy levels is located at E_V + 0.177 eV. After the scissors operation to overcome the band gap overestimation problem, the band gap of strontium-deficient $SrSO_4$ is adjusted to 7.6 eV; meanwhile, the peak of defect energy levels of strontium vacancy is adjusted to E_V + 0.175 eV.

The main motivation of the calculated band structures and densities of states of oxygen-deficient $SrSO_4$ and strontium-deficient $SrSO_4$ is to highlight the possible roles of oxygen and strontium vacancies in the PL and afterglow of undoped $SrSO_4$. The results in Figures 7 and 8 show that both the oxygen vacancy and the strontium vacancy can generate defect energy levels in the band gap of $SrSO_4$. On the one hand, the oxygen vacancy introduces one deep energy level (E_V + 2.50 eV) and one shallow energy level (E_V + 0.31 eV) in the band gap of $SrSO_4$. Since they are positively charged, they can work as electron traps. On the other hand, the strontium vacancy can generate shallow defect energy levels in the band gap of $SrSO_4$ (E_V + 0.175 eV). These strontium vacancies can work as hole traps because they are negatively charged. Apart from acting as carrier traps, these vacancies might be involved in the radiative recombination processes of undoped $SrSO_4$ nanoplates. Therefore, both the oxygen vacancies and the strontium vacancies might play important roles in the PL and afterglow of undoped $SrSO_4$. As discussed in the following section, comparison of the experimental data with the calculated electronic structures can unveil that the oxygen vacancy acts not only as the luminescence center of PL but also as a trap center and a luminescence center of afterglow.

2.6. Possible PL and Afterglow Mechanisms of Undoped $SrSO_4$. The possible PL and afterglow mechanisms of undoped $SrSO_4$ are illustrated in Figure 9. The band gap of

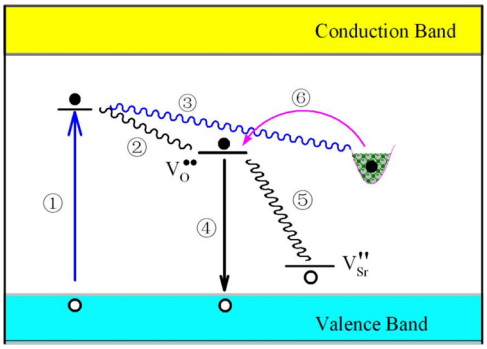

Figure 9. Schematic illustration of the PL and afterglow mechanisms of undoped $SrSO_4$. Process ①: absorption of the excitation energy by various kinds of intrinsic defects in the $SrSO_4$ lattice. Process ②: non-radiative relaxation of hot electrons to oxygen vacancies in the $SrSO_4$ lattice. Process ③: non-radiative relaxation of hot electrons to electron traps (oxygen vacancies) in the $SrSO_4$ lattice. Process ④: radiative recombination of electrons captured at the oxygen vacancy with holes in the valence band of $SrSO_4$, which results in a broad PL band. Process ⑤: radiative recombination of electrons captured at oxygen vacancies with holes captured at strontium vacancies, yielding another PL band. Process ⑥: thermal release of electrons from the traps in $SrSO_4$, and the subsequent radiative recombination *via* process ⑤ results in the cyan-colored afterglow.

$SrSO_4$ is assumed to be 7.6 eV.[22] As shown in Figure 9, one of the defect energy levels of oxygen vacancy is located at E_V + 2.50 eV, while the other defect energy level of oxygen vacancy, which is located at E_V + 0.31 eV, is not shown in Figure 9 for the purpose of clarity. Similarly, the defect energy level of strontium vacancy is located at E_V + 0.175 eV. Upon the excitation of the ultraviolet photons with a wavelength of 325 nm (3.82 eV), the $SrSO_4$ lattice can absorb some excitation

https://doi.org/10.1021/acsomega.1c00194
ACS Omega 2021, 6, 10129−10140

energy due to the presence of various kinds of intrinsic defects in practical $SrSO_4$ (process ①). After non-radiative relaxation, the hot electrons can be captured either by oxygen vacancies in the $SrSO_4$ lattice (process ②) or by electron traps present in $SrSO_4$ (process ③). In the case of our undoped $SrSO_4$, the electron traps are the oxygen vacancies themselves because, qualitatively speaking, the oxygen vacancies in $SrSO_4$ can work simultaneously as electron traps, the luminescence center of PL, and the luminescence center of afterglow.[12,13] After the capture of electrons at oxygen vacancies, the electrons can recombine radiatively with holes in the valence band of $SrSO_4$, resulting in a PL band peaking at about 2.50 eV, provided that the defect energy levels of oxygen vacancy are accurately located at E_V + 2.50 eV (process ④). Such an emission band corresponds to the PL band peaking at about 496 nm, which is denoted here as PL band A* for the convenience of discussion. Besides the recombination with holes in the valence band, the electrons captured at the oxygen vacancy apparently have a certain possibility to recombine radiatively with holes trapped at strontium vacancies, yielding another PL band peaking at about 2.33 eV, provided that the defect energy level of strontium vacancy is accurately located at E_V + 0.175 eV (process ⑤). Such a PL band corresponds to a PL band peaking at about 523 nm, which is denoted as PL band B*.

When comparing the PL bands A* and B* in Figure 9 with the two PL bands A and B in Figure 5, we can see that the peak energies of the PL bands A* (2.50 eV) and B* (2.33 eV) in Figure 9 are smaller than those of the two PL bands A (2.97 eV) and B (2.56 eV) in Figure 5. Theoretically speaking, the peak energies of the PL bands A* and B* in Figure 9 should be 2.97 and 2.56 eV, respectively, if our density functional theory calculations could give correct values of the defect energy levels for $SrSO_4$. Unfortunately, the density functional theory calculated values of the defect energy levels are underestimated. Such discrepancies between the calculated peak energies and the experimental peak energies of the two PL bands depend on the density functional theory itself. After having considered the not well-described band gaps of semiconductors and insulators in semilocal approximations to density functional theory, it is hard to reliably determine the defect energy levels within the band gap of $SrSO_4$.[28] That is the reason why the predicted peak energies of the two PL bands A* and B* in Figure 9 are 15.8 and 7.4% smaller than the actual peak energies of the two PL bands A and B in Figure 5.

The recorded two PL bands A and B in Figure 5 indicate that oxygen vacancies in $SrSO_4$ work as the luminescence center of PL upon the excitation of the ultraviolet laser. As illustrated in Figure 9, a portion of electrons can also be captured by the traps (oxygen vacancies) in the $SrSO_4$ lattice (process ③). These trapped electrons contribute nothing to the PL of $SrSO_4$ if they are not released from the traps. Once the ultraviolet excitation of the laser is stopped, processes ①–④ are ceased, but the electrons trapped at the positively charged traps (oxygen vacancies) begin their work. Under thermal activation, these trapped electrons can be released from the electron traps (process ⑥). Afterglow can be resulted *via* the recombination path ⑤ once the released electrons are captured by the luminescence center of PL (*i.e.*, oxygen vacancies). Hence, according to Figure 9, cyan-colored afterglow with weak intensity can be expected for undoped $SrSO_4$. Obviously, this afterglow mechanism involves the gradual release of electrons from electron traps (*i.e.*, oxygen vacancies), followed by electron migration to strontium vacancies. Therefore, the luminescence center of the afterglow of undoped $SrSO_4$ is the combination of oxygen vacancy and strontium vacancy. If so, the peak energy of the afterglow from undoped $SrSO_4$ is consequently determined by the energy difference between the defect energy levels of oxygen vacancy and strontium vacancy in the band gap of $SrSO_4$. If the proposed afterglow mechanism in Figure 9 is reasonable, the peak energy of the afterglow of undoped $SrSO_4$ should be equal to the peak energy of PL band B (2.56 eV) in Figure 5. In our case, the peak energy of the afterglow of undoped $SrSO_4$ (2.52 eV) is nearly equal to the peak energy of the PL band B in Figure 5 (2.56 eV). Although it would be better to exactly determine the absolute positions of these defect states in the band gap of $SrSO_4$ *via* the density functional calculations or *via* any reliable experimental techniques, it is currently not possible for us to do so due to a lot of limitations.

2.7. ESR Spectrum of Undoped $SrSO_4$. Electron spin resonance (ESR) spectroscopy is helpful in studying chemical species with unpaired electrons. Figure 10 illustrates the ESR spectrum of undoped $SrSO_4$ measured at room temperature. The microwave frequency was 9.856 GHz. From its crossover point, the center field of this resonance is determined to be 3515.5 G. Thus, the ESR spectrum in Figure 10 shows a signal at about 3515.5 G. This signal corresponds to a gyromagnetic g value of about 2.0031, which is very close to the g value of free electron (2.0023). The data in Figure 10 indicate that the undoped $SrSO_4$ contains unpaired electrons, which probably originate from electrons trapped in positively charged vacancies such as oxygen vacancies. Actually, such positively charged oxygen vacancies are present in a variety of inorganic materials such as $CaAl_2O_4$.[12]

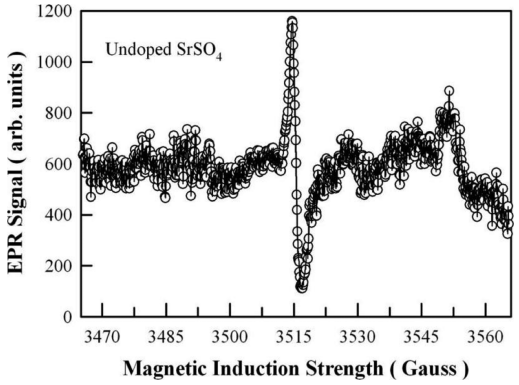

Figure 10. ESR spectrum of undoped $SrSO_4$ nanoplates measured at room temperature. Sweep width is 100 G. Microwave frequency: 9.856 GHz; microwave power: 20 mW; modulation frequency of the receiver: 100 Hz; and modulation amplitude of the receiver: 2 G.

2.8. Thermoluminescence Glow Curve of Undoped $SrSO_4$. Thermoluminescence is an important research tool to study the energy levels of impurity in solids.[29] Figure 11 represents the thermoluminescence glow curve of undoped $SrSO_4$. As shown in Figure 11, a broad thermoluminescence band peaking at about 40.1 °C (313.25 K) can be identified for undoped $SrSO_4$. This thermoluminescence band indicates that certain traps are present in undoped $SrSO_4$. In combination with the information derived from the PL and ESR measurements, these traps can be ascribed to the oxygen vacancies in the matrix of $SrSO_4$. The depths of the electron traps (or hole traps) are critically important to the duration of

https://doi.org/10.1021/acsomega.1c00194
ACS Omega 2021, 6, 10129−10140

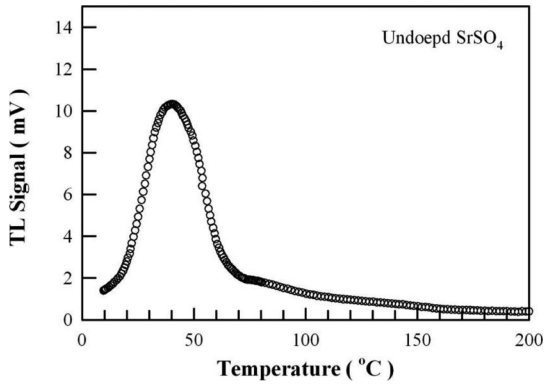

Figure 11. Thermoluminescence glow curve of undoped $SrSO_4$. The temperature rising rate was 2 °C/min.

afterglow. Generally speaking, shallow traps in afterglow materials can lead to an afterglow, which decays very quickly. As a contrast, afterglow materials with deep traps have long afterglow time. The trap depth can be calculated using the thermoluminescence glow curve.[30,31] Based on the shape of glow curve, we can calculate the trapping parameters with Chen's peak shape method. The geometry factor of the thermoluminescence glow curve, μ_g, is defined by eq 1

$$\mu_g = \frac{T_2 - T_m}{T_2 - T_1} \tag{1}$$

where T_m is the temperature at the maximum, T_1 is the half width temperature at the low-temperature side of the peak, and T_2 is the half width temperature at the high-temperature side of the peak. The readings of T_1, T_m, and T_2 in Figure 11 are 298.95, 313.25, and 329.75 K, respectively. Thus, the calculated value of the geometry factor is 0.5375 for the thermoluminescence glow curve of undoped $SrSO_4$ nanoplates. This value is very close to the value of μ_g = 0.52, which indicates the second-order kinetics of the thermoluminescence of undoped $SrSO_4$ nanoplates. Since the thermoluminescence glow curve exhibits second-order kinetics, a considerable amount of retrapping of charge carriers takes place in undoped $SrSO_4$ nanoplates. The trap depth in undoped $SrSO_4$ can be estimated using the following equation

$$E = 3.54\frac{kT_m^{\,2}}{T_2 - T_1} - 2kT_m \tag{2}$$

where E is the trap depth and k is Boltzmann's constant.[32,33] It is found that the trap depth is 0.918 eV for undoped $SrSO_4$ nanoplates. The calculated value of the trap depth in undoped $SrSO_4$ is indicative of the formation of traps in $SrSO_4$ nanoplates. Obviously, these traps are too shallow to give off sufficiently long afterglow for undoped $SrSO_4$ because a little amount of energy is needed to detrap the charge carriers from the trap centers. The corresponding frequency factor s (in the unit of s^{-1}), which is the frequency of an electron escaping the trap, can be calculated using the second-order kinetics formula as given in eq 3

$$s = \frac{\beta E}{kT_m^{\,2}}\frac{1}{1 + 2kT_m/E}\exp\left(\frac{E}{kT_m}\right) \tag{3}$$

The calculated value of the frequency factor is 1.2×10^{14} s^{-1}. In an attempt to escape from the potential well, the frequency factor represents the product of the number of times an electron hits the wall and the wall reflection coefficient when the trap is treated as a potential well. It is clear that the estimations of the trap depth and the frequency factor utilize the values of shape parameters (T_1, T_2, and T_m) along with geometry factor (μ_g). Lifetime is generally estimated using the equation

$$\tau = s^{-1}\exp\left(\frac{E}{kT}\right) \tag{4}$$

where E is the trap depth, s is the frequency factor, and k is Boltzmann's constant. The value of room-temperature lifetime of undoped $SrSO_4$ nanoplates is estimated to be 17.9 s, which can be utilized to justify the physical basis of the output parameters.

Doping a host material with rare-earth ions can enhance the trap depth and hence increase the peak temperature of the thermoluminescence glow curve.[34] For example, Atone et al. reported that the most prominent glow peak appears at 140 °C for their Tb-doped $SrSO_4$ phosphors after exposure to the irradiation of gamma rays;[35] Khadijeh et al. reported that the dominant glow peak is located at 217 °C for Dy- and Tb-codoped $SrSO_4$ after exposure to the irradiation of gamma ray.[36] The comparison of these thermoluminescence glow curves reveals that doping $SrSO_4$ with rare-earth ions is one effective method to enhance the trap depths in $SrSO_4$. Additionally, Ambast and Sharma reported that the trap depth in $CaWO_4$ varied by doping with Dy^{3+} alone or by codoping with Dy^{3+} and K^+.[37] The results indicate that trap depth varies after doping or codoping with specific dopants. Consequently, it is expected that doping $SrSO_4$ nanoplates can adjust the trap depth to a suitable value so that sufficiently long afterglow can be achieved. In addition to doping, both thermal annealing and high energy electron irradiation can control the population density of intrinsic defects in $SrSO_4$.[7,34,38] In the case of oxygen vacancy as the luminescence center of PL, the relative value of the population density of the oxygen vacancy can be measured through the PL intensity measurement, and the absolute value of the population density of the oxygen vacancy can be derived *via* the ESR technique.

2.9. Emission-Wavelength Dependence of Time-Resolved PL for Undoped $SrSO_4$ Nanoplates. As mentioned in Figure 9, the differences in the steady-state PL spectrum and the afterglow spectrum are explained in terms of the presence of multiple luminescence paths in undoped $SrSO_4$. It is known that investigation of time-resolved PL can offer important information on the luminescence paths in a diversity of materials.[5,8,23,24,39] In the light of the mechanisms proposed in Figure 9, there should be three relaxation paths, at least, for the excited carriers in undoped $SrSO_4$, and the PL lifetime of the carriers will depend on the emission wavelength. In order to study the recombination dynamics in undoped $SrSO_4$ nanoplates, we measured the time-resolved PL spectra at different detection wavelengths when the excitation wavelength was fixed at 375 nm. Figure 12 represents the time-resolved PL spectra of undoped $SrSO_4$ nanoplates at detection wavelengths of 418 nm (a) and 485 nm (b). The two detection wavelengths are close to the peaks of the PL bands A and B in Figure 5. Indeed, the PL decay profile of undoped $SrSO_4$ is heavily dependent on the emission wavelength, as can be seen in Figure 12. Detailed analysis shows that each PL decay curve in Figure 12 can be fitted with one quadruple exponential function

https://doi.org/10.1021/acsomega.1c00194
ACS Omega 2021, 6, 10129−10140

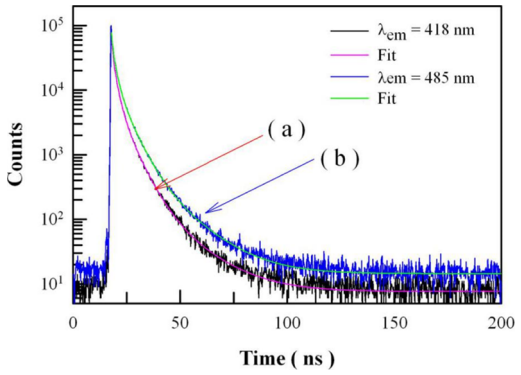

Figure 12. Time-resolved PL spectra of undoped $SrSO_4$ at different detection wavelengths: (a) λ_{em} = 418 nm and (b) λ_{em} = 485 nm. The excitation wavelength is fixed at 375 nm.

$$I(t) = A_o + \sum_{i=1}^{n} A_i \exp(-t/\tau_i) \quad (5)$$

where $I(t)$ refers to the PL intensity at time t, A_0 is the baseline, A_i is the pre-exponential factor of the ith decay component, and τ_i is the decay time constant of the ith decay component (i = 1−4).[23,39] The fitting parameters τ_i and I_i (i = 1−4) of the time-resolved PL spectra in Figure 9 are listed in Table 1. The parameter χ^2 in Table 1 represents the goodness of fit, and the average lifetime, τ_{avg}, is calculated by using the formula

$$\tau_{avg} = \left(\sum_{i=1}^{n} A_i \tau_i^2\right) / \left(\sum_{i=1}^{n} A_i \tau_i^2\right) \quad (6)$$

These fitting parameters bear important information on the kinetics of carrier recombination. The most prominent feature of the data in Table 1 is that there are four decay components for each time-resolved PL spectrum in Figure 12. For example, the four decay time constants are τ_1 = 0.51 ns, τ_2 = 1.88 ns, τ_3 = 5.59 ns, and τ_4 = 15.97 ns for $SrSO_4$ when the detection wavelength is 418 nm. It is noted that τ_1 is at the limit of the measurement capability of the instrument, and therefore, it merely represents the order of the short decay time constant.[5,23,25,39] Consequently, the time-resolved PL spectra in Figure 12 suggest that there are three independent radiative relaxation paths that contribute to the blue emissions of the undoped $SrSO_4$. As discussed in Figure 9, the three different relaxation paths in undoped $SrSO_4$ nanoplates are correlated to processes ④ and ⑤ and the combined process ⑥ and ⑤. The second prominent feature of the data in Table 1 is the increase in the average lifetime with increasing detection wavelength. As listed in Table 1, the weighed average lifetimes are calculated to be 3.52 and 4.40 ns for the detection wavelengths of 418 and 485 nm, respectively. Obviously, the average lifetime of the visible emission at 485 nm (4.40 ns) is much longer than that of the emission at 418 nm (3.52 ns). Similar emission-wavelength-dependent lifetime was reported for undoped $CaAl_2O_4$ nanocrystals.[12] As documented in the literature, this is the characteristic of emissions involving deep trap states.[40,41] Therefore, the emission-wavelength-dependent PL decay suggests that the emissions involved deep trap states in $SrSO_4$.

2.10. Excitation-Wavelength Dependence of Time-Resolved PL for Undoped $SrSO_4$ Nanoplates. It is proved that the luminescence lifetime is also dependent on the excitation wavelength if multiple luminescence centers are present.[42] Thus, we investigated the charge carrier dynamics of the relaxation processes in undoped $SrSO_4$ nanoplates by measuring the time-resolved PL at different excitation wavelengths when the detection wavelength is fixed at 418 nm. Figure 13 represents the time-resolved PL spectra of undoped $SrSO_4$ nanoplates at excitation wavelengths of 255, 320, and 375 nm. The detection wavelength is fixed at 418 nm. It is found that the PL decay curves a and b can be reasonably fitted with one triple exponential function while the PL decay curve c can only be fitted with one quadruple exponential function. Table 2 lists the fitting parameters of each time-

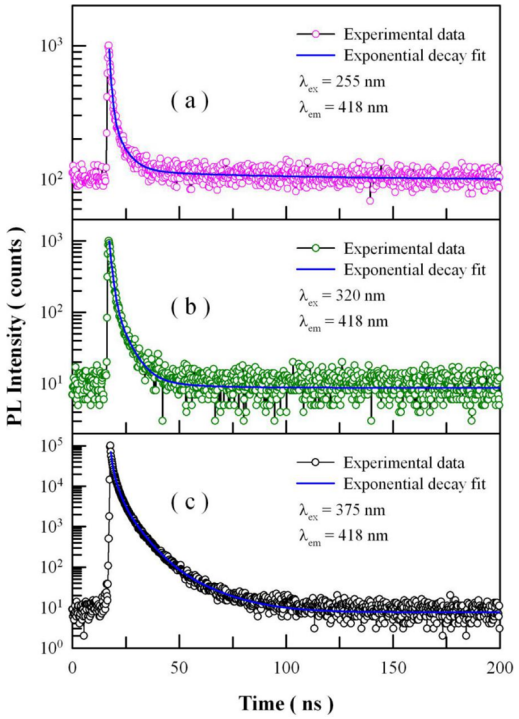

Figure 13. Time-resolved PL spectra of undoped $SrSO_4$ at different excitation wavelengths: (a) λ_{ex} = 255 nm, (b) λ_{ex} = 320 nm, and (c) λ_{ex} = 375 nm. The detection wavelength is fixed at 418 nm.

Table 1. Fitting Parameters of the Time-Resolved PL Spectra of Undoped $SrSO_4$ Nanoplates with Different Detection Wavelengths When the Excitation Wavelength Is Fixed at 375 nm

excitation wavelength (nm)	detection wavelength (nm)	A_0	I_1 τ_1 (ns)	I_2 τ_2 (ns)	I_3 τ_3 (ns)	I_4 τ_4 (ns)	τ_{ave} (ns)	χ^2
375	418	7.63	47139.8	32818.5	8114.1	401.2	3.52	1.153
			0.51	1.88	5.59	15.97		
375	485	14.43	40532.4	40611.6	14262.1	1106.4	4.40	1.247
			0.46	1.77	5.49	15.07		

https://doi.org/10.1021/acsomega.1c00194
ACS Omega 2021, 6, 10129−10140

Table 2. Fitting Parameters of the Time-Resolved PL Spectra of Undoped $SrSO_4$ Nanoplates with Different Excitation Wavelengths When the Detection Wavelength Is Fixed at 418 nm

excitation wavelength (nm)	detection wavelength (nm)	A_0	I_1 τ_1 (ns)	I_2 τ_2 (ns)	I_3 τ_3 (ns)	I_4 τ_4 (ns)	$\langle\tau\rangle$ (ns)	χ^2
255	418	99.116	727.60	221.97	17.64	none	35.89	1.072
			1.08	5.60	81.24	none		
320	418	8.758	956.40	167.69	4.51	none	3.80	1.036
			1.25	5.35	21.17	none		
375	418	7.63	47139.8	32818.5	8114.1	401.2	3.52	1.153
			0.51	1.88	5.59	15.97		

resolved PL spectrum in Figure 13. Apparently, the most notable difference in the PL decays rests on the number of exponential components. As discussed above, the number of radiative recombination paths is 2 when the excitation wavelengths are 255 and 320 nm, respectively. As a sharp contrast, the number of radiative recombination paths is 3 when the excitation wavelength is 375 nm. The second prominent feature of the data in Table 2 is the decrease in the average lifetime with increasing excitation wavelength. As can be seen in Table 2, the average lifetimes of the carriers in undoped $SrSO_4$ nanoplates are 35.89, 3.80, and 3.52 ns for the excitation wavelengths of 255, 320, and 375 nm, respectively. It is clear that the average lifetime of the PL is longer at shorter excitation wavelengths but shorter at longer excitation wavelengths. These data indicate that the time-resolved PL spectrum of undoped $SrSO_4$ nanoplates is excitation-wavelength-dependent.

The average lifetimes in Table 2 contain important information on the energy spacing of the defects involved in the blue emissions from undoped $SrSO_4$ nanoplates. Since the PL band A peaking at 418 nm is associated with the defect emissions in undoped $SrSO_4$ nanoplates, the nature of the PL decay of these defect emissions is generally determined by the energy spacing between the defects associated with the blue emissions. In other words, defects that are close in energy space have a faster decay, while those with larger spacing in energy space have a slower decay.[42] Here, we suppose that the energy level of oxygen vacancy of $SrSO_4$ is located at 2.97 eV above the valence band, as shown in Figure 9. Upon the excitation of 255 nm photons (4.86 eV), only those defects at E_V + 4.86 eV can absorb the excitation energy of the incoming photons. In this case, the absorption species is 1.89 eV above the luminescence center (oxygen vacancies) in energy space. Similarly, the absorption species is only 0.34 eV above the luminescence center (oxygen vacancies) in energy space upon the excitation of 375 nm photons (3.31 eV). Due to the larger energy difference in the former case, it takes much longer time for the excited electron to complete its non-radiative relaxation process ② than the latter case. Consequently, the blue emission at 418 nm decays very fast upon the excitation of 375 nm, while this PL decays much more slowly upon the excitation of 255 nm.

3. SUMMARY

$SrSO_4$ nanoplates are derived *via* the composite hydroxide-mediated approach at 240 °C. These phosphors are characterized in detail by means of XRD, SEM, EDX, XPS, steady-state PL, time-resolved PL, and afterglow spectroscopies and thermoluminescence dosimetry. The steady-state PL spectrum of undoped $SrSO_4$ nanoplates can be deconvoluted into two Gaussian bands centered at 2.97 eV (417.2 nm) and 2.56 eV (484.4 nm), respectively. The cyan-colored afterglow peaking at about 492 nm (2.52 eV) is recorded in the undoped $SrSO_4$ material upon ultraviolet laser irradiation (325 nm, 13 mW). The duration of the afterglow is measured to be 16 s. The thermoluminescence glow curve of undoped $SrSO_4$ nanoplates exhibits a peak at about 40.1 °C, and the trap depth is estimated to be about 0.918 eV using the peak shape method. In order to shed light on the origins of the blue PL and the cyan-colored afterglow, density functional theory calculations are performed to derive the band structures and densities of states for oxygen-deficient $SrSO_4$ and strontium-deficient $SrSO_4$. It turns out that both the oxygen vacancies and the strontium vacancies in the lattice of $SrSO_4$ play important roles in the cyan-colored afterglow of undoped $SrSO_4$ nanoplates. The emission wavelength- and the excitation wavelength-dependent PL decays are studied to investigate the nature of defect emissions in $SrSO_4$ nanoplates. Our results demonstrate that (i) the blue emission at 418 nm decays much faster (3.52 ns) than the blue emission at 485 nm does (4.40 ns) when the excitation wavelength is fixed at 375 nm and (ii) the blue emission decays slower (35.89 ns) at shorter excitation wavelength (255 nm) but faster (3.52 ns) at longer excitation wavelength (375 nm) when the emission wavelength is fixed at 418 nm. These PL decay characteristics are indicative of the nature of defect emissions of undoped $SrSO_4$ nanoplates. These data have demonstrated the triple roles played by oxygen vacancies in undoped $SrSO_4$: (i) they work as the luminescence center of PL to be responsible for the blue emissions; (ii) they work as the luminescence center of afterglow to account for the cyan-colored afterglow; and (iii) they act as the carrier traps to be responsible for the accumulation of charge carriers at room temperature. Our findings can not only provide a comprehensive understanding on the PL and afterglow of undoped $SrSO_4$ but also present an alternative strategy toward designing new afterglow materials through the examination of undoped inorganic materials.

4. EXPERIMENTAL SECTION

4.1. Synthesis of $SrSO_4$ Nanoplates. $SrSO_4$ nanoplates were synthesized *via* the composite hydroxide-mediated approach.[16,17] All chemicals used in this work were provided by Sinopharm Chemical Reagents Ltd (Shanghai, China). Analytical reagents NaOH (0.515 mol) and KOH (0.485 mol) were thoroughly mixed in a clean beaker to form the composite hydroxides in order to form eutectic melts at 165 °C and above. Analytical reagents $Sr(NO_3)_2$ and Na_2SO_4 were used as the starting materials to form $SrSO_4$ nanoplates. $Sr(NO_3)_2$ (0.1 mol) and Na_2SO_4 (0.1 mol) were mixed into the composite hydroxides. The mixture was filled into a Teflon vessel (with a capacity of 100 mL). After covering with a Teflon lid, the Teflon vessel was put in a furnace for chemical reactions. The

https://doi.org/10.1021/acsomega.1c00194
ACS Omega 2021, 6, 10129−10140

temperature in the furnace was set at 240 °C. After reacting for 24 h, the vessel was taken out of the furnace. The solid product in the vessel was dissolved in deionized water. The $SrCO_3$ impurity in the solids was removed by washing with dilute hydrochloric acid. After repeated washing with deionized water to remove the composite hydroxides on the surface of the particles, the solids were filtered and dried in an oven overnight.

4.2. Phase, Morphology, Elemental Composition, and Chemical State of $SrSO_4$ Nanoplates. The X-ray diffraction (XRD) profiles of undoped $SrSO_4$ nanoplates were recorded on an X-ray diffractometer (D/max 2500 PC, Rigaku Corporation, Akishima, Japan) using Cu Kα radiation (λ = 0.15405 nm). A scanning electron microscope (model S-4800, Hitachi, Tokyo, Japan) was employed to analyze the morphology of the synthesized products. The scanning electron microscope was coupled with a silicon-drifted detector as the X-ray analyzer to record the energy-dispersive X-ray (EDX) spectrum of the synthesized products. X-ray photoelectron spectroscopy (XPS) analysis was carried out on an Escalab 250Xi spectrophotometer (Thermo Scientific, Waltham, MA, USA). The incident X-ray came from Al Kα radiation with an energy of 1486.6 eV.

4.3. Steady-State PL and Time-Resolved PL Spectra of Undoped $SrSO_4$. A spectrophotometer (Tianjin Gangdong Ltd., Tianjin, China) was used to acquire the steady-state PL spectra of undoped $SrSO_4$. The excitation source of the PL measurement was provided by a helium−cadmium laser (Kimmon Electric Co. Ltd., Tokyo, Japan). The wavelength of laser radiation was 325 nm, and the output power of the laser radiation was 13 mW. The time-resolved PL spectra of the $SrSO_4$ nanoplates were obtained at room temperature on a picosecond fluorescence lifetime spectrometer (LifeSpec II, Edinburgh Instruments, Edinburgh, UK) utilizing a time-correlated single-photon counting method with a pulsed light source. Two picosecond pulsed light-emitting diodes and one pulsed diode laser were employed in this work to provide emission wavelengths of 255, 320, and 375 nm with an average power of 0.3 μW, 0.8 μW, and 0.1 mW, respectively. Their pulse widths at an operating repetition frequency of 5 MHz were 900, 700, and 90 ps, correspondingly. Details on the time-resolved PL analyses could be found elsewhere.[43,44] All the measurements were carried out at room temperature.

4.4. ESR Measurement of Undoped $SrSO_4$. The X-band ESR spectrum was measured at room temperature using an X-band ESR spectrometer (Bruker E500) with a 100 kHz magnetic field modulator. The settings of the ESR spectrometer were as follows: the center field was 3515.5 G and the sweep width was 100 G. The resonance frequency of its cavity was 9.856 GHz. The modulation frequency of its receiver is 100 Hz, while the modulation amplitude of the receiver is 2 G.

4.5. Afterglow Spectrum and Thermoluminescence Glow Curve of Undoped $SrSO_4$. The afterglow spectrum of undoped $SrSO_4$ was recorded with the same PL spectrophotometer (Tianjin Gangdong Ltd., Tianjin, China) after the laser irradiation was blocked off. The thermoluminescence glow curves of undoped $SrSO_4$ were measured on a thermoluminescence meter constructed according to the scheme given by Yamashita et al.[45] Prior to the thermoluminescence measurements, undoped $SrSO_4$ nanoplates were exposed to the irradiation of ultraviolet light of 254 nm for 10 min. The thermoluminescence signals of undoped $SrSO_4$ nanoplates were recorded when $SrSO_4$ was heated from 10 to 200 °C at a rate of 2 °C/s.

4.6. Electronic Structure Calculations of $SrSO_4$ Nanoplates. First-principles density functional calculations of the band structures and the densities of states of $SrSO_4$ were performed using the density functional theory module of the Quantumwise Atomistix ToolKit 11.8 (Atomistix ToolKit 11.8 package, Copenhagen, Denmark). The exchange−correlation functional was treated within the generalized gradient approximation (GGA) + U scheme by the Perdew−Burke−Ernzerhof potential.[46] The U parameter was selected as U^{2p} = 4 eV for oxygen. Orthorhombic $SrSO_4$ belonged to the space group *Pnma* (62). The unit cell of $SrSO_4$ consisted of 4 Sr atoms, 4 S atoms, and 16 O atoms. The initial structural data of $SrSO_4$ were taken from the Inorganic Crystal Structure Database (ICSD) with the ICSD number of 85808. The lattice parameters of a = 0.8359 nm, b = 0.5351 nm, and c = 0.6869 nm were used in the present work. The considered electronic configurations were $3d^{10}4p^{6}5s^{2}$ for Sr, $2s^{2}2p^{4}$ for O, and $3s^{2}3p^{4}$ for S. A 2 × 2 × 1 supercell was constructed for the oxygen-deficient $SrSO_4$. Such a supercell consisted of 16 Sr sites, 16 S sites, and 64 O sites. When one oxygen site was vacant, oxygen-deficient $SrSO_4$ resulted. The resultant $SrSO_4$ was denoted as $SrSO_{4-\delta}$ in this work, where δ = 0.0625. Similarly, Sr-deficient $SrSO_4$ resulted after the removal of one strontium site from the supercell. The resultant $SrSO_4$ was denoted as $Sr_{1-\delta}SO_4$ in this work, where δ = 0.0625. Double-zeta single-polarized basis sets were chosen for each element. The electronic wave functions were expanded in plane waves up to a typical kinetic energy cutoff value of 125 Hartree. The Monkhorst−Pack scheme k-point grid sampling was set at 5 × 5 × 5 for the Brillouin zone. The Brillouin zone sampling and the kinetic energy cutoff were sufficient to guarantee an excellent convergence for the calculated band structures. Details on the density functional calculations were available elsewhere.[12−14,47]

■ ASSOCIATED CONTENT

Supporting Information

The Supporting Information is available free of charge at https://pubs.acs.org/doi/10.1021/acsomega.1c00194.

Afterglow photos of undoped $SrSO_4$ after annealing at different temperatures for 2 h and PL spectra of undoped $SrSO_4$ nanoplates measured at different temperatures on a heating console (PDF)

■ AUTHOR INFORMATION

Corresponding Author

Yuan Ming Huang − *School of Microelectronics and Control Engineering, Changzhou University, Changzhou 213164, China*; orcid.org/0000-0002-6353-9201; Email: dongshanisland@126.com

Authors

Bao-gai Zhai − *School of Microelectronics and Control Engineering, Changzhou University, Changzhou 213164, China*

Hanfei Xu − *School of Microelectronics and Control Engineering, Changzhou University, Changzhou 213164, China*

Qing Zhang − *School of Microelectronics and Control Engineering, Changzhou University, Changzhou 213164, China*

Complete contact information is available at: https://pubs.acs.org/10.1021/acsomega.1c00194

Notes

The authors declare no competing financial interest.

■ ACKNOWLEDGMENTS

The financial support received from the National Natural Science Foundation of China (nos. 11574036 and 11604028) was acknowledged.

■ REFERENCES

(1) Hölsä, J. Persistent luminescence beats the afterglow: 400 years of persistent luminescence. *Electrochem. Soc. Interface* **2009**, *18*, 42−45.
(2) Matsuzawa, T.; Aoki, Y.; Takeuchi, N.; Murayama, Y. A New Long Phosphorescent Phosphor with High Brightness, $SrAl_2O_4$: Eu^{2+}, Dy^{3+}. *J. Electrochem. Soc.* **1996**, *143*, 2670−2673.
(3) Van den Eeckhout, K.; Smet, P. F.; Poelman, D. Persistent Luminescence in Eu^{2+}-Doped Compounds: A Review. *Materials* **2010**, *3*, 2536−2566.
(4) Zhai, B.-g.; Yang, L.; Ma, Q.-l.; Liu, X.; Huang, Y. M. Mechanism of the prolongation of the green afterglow of $SrAl_2O_4$:Dy^{3+} caused by the use of H_3BO_3 flux. *J. Lumin.* **2017**, *181*, 78−87.
(5) Huang, Y. M.; Ma, Q.-l. Long afterglow of trivalent dysprosium doped strontium aluminate. *J. Lumin.* **2015**, *160*, 271−275.
(6) Zhai, B.-g.; Huang, Y. M. Green photoluminescence and afterglow of Tb-doped $SrAl_2O_4$. *J. Mater. Sci.* **2017**, *52*, 1813−1822.
(7) Smet, P. F.; Avci, N.; Van den Eeckhout, K.; Poelman, D. Extending the afterglow in $CaAl_2O_4$:Eu,Nd persistent phosphors by electron beam annealing. *Opt. Mater. Express* **2012**, *2*, 1306−1313.
(8) Zhai, B.-g.; Ma, Q.-l.; Xiong, R.; Li, X.; Huang, Y. M. Blue-green afterglow of $BaAl_2O_4$:Dy^{3+} phosphors. *Mater. Res. Bull.* **2016**, *75*, 1−6.
(9) Wiatrowska, A.; Zych, E.; Kępiński, L. Monoclinic HfO_2:Eu X-ray phosphor. *Radiat. Meas.* **2010**, *45*, 493.
(10) Pejaković, D. A. Studies of the phosphorescence of polycrystalline hafnia. *J. Lumin.* **2010**, *130*, 1048−1054.
(11) Behrh, G. K.; Isobe, M.; Massuyeau, F.; Serier-Brault, H.; Gordon, E. E.; Koo, H.-J.; Whangbo, M.-H.; Gautier, R.; Jobic, S. Oxygen-Vacancy-Induced Midgap States Responsible for the Fluorescence and the Long-Lasting Phosphorescence of the Inverse Spinel $Mg(Mg,Sn)O_4$. *Chem. Mater.* **2017**, *29*, 1069.
(12) Zhai, B.-g.; Huang, Y. M. Blue afterglow of undoped $CaAl_2O_4$ nanocrystals. *Europhys. Lett.* **2019**, *127*, 17001.
(13) Zhai, B.-g.; Xu, H.; Zhuo, F.; Huang, Y. M. Annealing temperature dependent photoluminescence and afterglow of undoped $CaAl_2O_4$. *J. Alloys Compd.* **2020**, *821*, 153563.
(14) Zhai, B.-g.; Liu, D.; He, Y.; Yang, L.; Huang, Y. M. Tuning the photoluminescence of Eu^{2+} and Eu^{3+} co-doped $SrSO_4$ through post annealing technique. *J. Lumin.* **2018**, *194*, 485−493.
(15) Di, Q.; Han, L.; Xu, Q.; Sun, G.; Sun, J. Hydrothermal approach for the shape-selective $SrSO_4$:Eu^{2+} microcrystals and its luminescence properties. *Appl. Phys. A* **2015**, *118*, 961−966.
(16) Hu, C.; Xi, Y.; Liu, H.; Wang, Z. L. Composite-hydroxide-mediated approach as a general methodology for synthesizing nanostructures. *J. Mater. Chem.* **2009**, *19*, 858−868.
(17) Zhai, B.-G.; Ma, Q.-l.; Yang, L.; Huang, Y. M. Synthesis of morphology-tunable ZnO nanostructures via the composite hydroxide mediated approach for photocatalytic applications. *Mater. Res. Express* **2016**, *3*, 105045.
(18) Zhai, B.-g.; Ma, Q.-l.; Huang, Y. M. Instability of the characteristic emissions of dopant Tb in ZnO hexagonal pyramids. *J. Electron. Mater.* **2017**, *46*, 947−954.
(19) Vasquez, R. P. $SrSO_4$ by XPS. *Surf. Sci. Spectra* **1992**, *1*, 117−121.
(20) Vasquez, R. P. X-ray photoelectron spectroscopy study of Sr and Ba compounds. *J. Electron Spectrosc. Relat. Phenom.* **1991**, *56*, 217−240.
(21) Ma, Q.-l.; Xiong, R.; Huang, Y. M. Tunable photoluminescence of porous silicon by liquid crystal infiltration. *J. Lumin.* **2011**, *131*, 2053−2057.
(22) Amiryan, A. M.; Gurvieh, A. M.; Katomina, R. V.; Petrova, I. Y.; Soshchin, N. P.; Tombak, M. I. Recombination processes and emission spectrum of terbium in oxysulfides. *J. Appl. Spectrosc.* **1977**, *27*, 1159−1162.
(23) Zhai, B.-g.; Yang, L.; Huang, Y. M. Intrinsic Defect Engineering in Eu^{3+} Doped $ZnWO_4$ for Annealing Temperature Tunable Photoluminescence. *Nanomaterials* **2019**, *9*, 99.
(24) Zhai, B.-g.; Yang, L.; Zhou, F.-f.; Shi, J.-s.; Huang, Y. M. Strong Photo-Oxidative Capability of $ZnWO_4$ Nanoplates with Highly Exposed {0 1 1} Facets. *Catalysts* **2019**, *9*, 178.
(25) Zhai, B.-g.; Ma, Q.-l.; Yang, L.; Huang, Y. M. Growth of $ZnMoO_4$ nanowires via vapor deposition in air. *Mater. Lett.* **2017**, *188*, 119−122.
(26) Zhou, Z.; Jiang, K.; Chen, N.; Xie, Z.; Lei, B.; Zhuang, J.; Zhang, X.; Liu, Y.; Hu, C. Room temperature long afterglow from boron oxide: A boric acid calcined product. *Mater. Lett.* **2020**, *276*, 128226.
(27) Hu, Z.; Zhang, C.; Li, Y.; Ao, B. First-principles study of structural, electronic, optical and bonding properties of celestine, $SrSO_4$. *Solid State Commun.* **2013**, *158*, 5−8.
(28) Chen, W.; Pasquarello, A. First-principles determination of defect energy levels through hybrid density functionals and GW. *J. Phys. Condens. Matter* **2015**, *27*, 133202.
(29) Bos, A. Thermoluminescence as a research tool to investigate luminescence mechanisms. *Materials* **2017**, *10*, 1357.
(30) Chen, R. Glow curves with general order kinetics. *J. Electrochem. Soc.* **1969**, *116*, 1254−1257.
(31) Chen, R. On the calculation of activation energies and frequency factors from glow curves. *J. Appl. Phys.* **1969**, *40*, 570−585.
(32) Wako, A. H.; Dejene, F. B.; Swart, H. C. Trap characteristics of UV-activated $Y_3(Al,Ga)_5O_{12}$:Ce^{3+} phosphors. *Optik* **2016**, *127*, 3918−3924.
(33) Manam, J.; Sharma, S. K. Determination of trapping parameters from thermally stimulated luminescence glow curves of Mn−doped $Li_2B_4O_7$ phosphor. *Radiat. Eff. Defect Solid* **2008**, *163*, 813−819.
(34) Zhai, B.-g.; Xu, H.; Huang, Y. M. Annealing temperature dependent afterglow of Tb^{3+} doped $CaAl_2O_4$. *Opt. Mater.* **2021**, *112*, 110739.
(35) Atone, M. S.; Moharil, S. V.; Dhopte, S. M.; Muthal, P. L.; Kondawar, V. K. Synthesis and Characterization of $SrSO_4$:Mo, Tb Thermoluminescent Phosphor. *Phys. Status Solidi A* **1999**, *174*, 521−526.
(36) Khadijeh, R. E. S.; Amin, A. K.; Maryam, E. Synthesis, characterization and TL properties of $SrSO_4$:Dy,Tb nanocrystalline phosphor. *J. Rare Earths* **2014**, *32*, 1003−1009.
(37) Ambast, A. K.; Sharma, S. K. Variation of trap depth by dopant/codopant and heating rate in $CaWO_4$ phosphors. *Opt. Quant. Electron.* **2017**, *49*, 58.
(38) Novoselov, I. I.; Savin, D. I.; Yanilkin, A. V. The effect of irradiation conditions on generation of defects and their clusters. *J. Nucl. Mater.* **2021**, *546*, 152762.
(39) Huang, Y. M.; Li, M.; Yang, L.; Zhai, B.-g. Eu^{2+} and Eu^{3+} Doubly Doped ZnWO4 Nanoplates with Superior Photocatalytic Performance for Dye Degradation. *Nanomaterials* **2018**, *8*, 765.
(40) Rakshit, S.; Vasudevan, S. Trap-State Dynamics in Visible-Light-Emitting ZnO:MgO Nanocrystals. *J. Phys. Chem. C* **2008**, *112*, 4531−4537.
(41) Brus, L. Electronic wave functions in semiconductor clusters: experiment and theory. *J. Phys. Chem.* **1986**, *90*, 2555−2560.
(42) Yakami, B. R.; Poudyal, U.; Nandyala, S. R.; Rimal, G.; Cooper, J. K.; Zhang, X.; Wang, J.; Wang, W.; Pikal, J. M. Steady state and

time resolved optical characterization studies of Zn_2SnO_4 nanowires for solar cell applications. *J. Appl. Phys.* **2016**, *120*, 163101.
(43) Zhai, B.-g.; Ma, Q.-l.; Yang, L.; Huang, Y. M. Synthesis and optical properties of Tb-doped pentazinc dimolybdate pentahydrate. *Results Phys.* **2017**, *7*, 3991−4000.
(44) Zhai, B.-g.; Ma, Q.-l.; Yang, L.; Huang, Y. M. Effects of sintering temperature on the morphology and photoluminescence of Eu^{3+} doped zinc molybdenum oxide hydrate. *J. Nanomater.* **2018**, *2018*, 7418508.
(45) Yamashita, N.; Hamada, T.; Takada, M.; Katsuki, M.; Nakagawa, M. Photoluminescence and Thermoluminescence of $MgSO_4$, $CaSO_4$, $SrSO_4$ and $BaSO_4$ Powder Phosphors Activated with Tb^{3+}. *Jpn. J. Appl. Phys.* **2001**, *40*, 6732−6736.
(46) Perdew, J. P.; Burke, K.; Ernzerhof, M. Generalized gradient approximation made simple. *Phys. Rev. Lett.* **1996**, *77*, 3865−3868.
(47) Chen, L.-l.; Zhai, B.-g.; Huang, Y. M. Rendering Visible-Light Photocatalytic Activity to Undoped ZnO via Intrinsic Defects Engineering. *Catalysts* **2020**, *10*, 1163.

https://doi.org/10.1021/acsomega.1c00194
ACS Omega 2021, 6, 10129−10140